MICROTECHNOLOGY

Acoustic tweezers via sub–time-of-flight regime surface acoustic waves

10.1126/sciadv.1600089

David J. Collins,[1] Citsabehsan Devendran,[2] Zhichao Ma,[1] Jia Wei Ng,[2] Adrian Neild,[2]* Ye Ai[1]*

Micrometer-scale acoustic waves are highly useful for refined optomechanical and acoustofluidic manipulation, where these fields are spatially localized along the transducer aperture but not along the acoustic propagation direction. In the case of acoustic tweezers, such a conventional acoustic standing wave results in particle and cell patterning across the entire width of a microfluidic channel, preventing selective trapping. We demonstrate the use of nanosecond-scale pulsed surface acoustic waves (SAWs) with a pulse period that is less than the time of flight between opposing transducers to generate localized time-averaged patterning regions while using conventional electrode structures. These nodal positions can be readily and arbitrarily positioned in two dimensions and within the patterning region itself through the imposition of pulse delays, frequency modulation, and phase shifts. This straightforward concept adds new spatial dimensions to which acoustic fields can be localized in SAW applications in a manner analogous to optical tweezers, including spatially selective acoustic tweezers and optical waveguides.

INTRODUCTION

Surface acoustic waves (SAWs) are an efficient tool for microscale manipulation in diverse applications, including optical scattering, waveguides and computing (*1*–*5*), telecommunications (*6*), sensing (*7*), and microscale manipulation (*8*, *9*). A standing SAW field results in time-averaged nodal and antinodal positions on the substrate and fluids into which it couples and is readily generated on planar piezoelectric substrates by an AC signal applied to opposing sets of interdigital transducers (IDTs). However, this standing wave develops across the entire inter-IDT space, preventing localized manipulation in a manner analogous to optical tweezers. The term "acoustic tweezers" has been applied to microfluidic systems using SAW (*10*, *11*), but the imposition of this field results in cell and particle patterning in the entirety of a microfluidic channel, although phased array bulk acoustic wave (BAW) transducers are capable of generating nonuniform acoustic patterns using several piezoelectric elements (*12*, *13*). Here, we demonstrate the straightforward application of nanosecond-scale SAW pulses in a sub–time-of-flight (sub-TOF) regime, where the locations and dimensions of the localized standing wave regions in the substrate are determined by the TOF and pulse length of a SAW, and where only two sets of transducers are required. In recent work, Fourier synthesis has been used to shape the time-averaged substrate waveforms (*14*), although pulsed SAW has not been previously used to generate spatially localized standing wave patterning. The time-averaged field resulting from intersecting SAW pulses yields discrete standing wave locations in a coupled fluid independent of channel dimensions. This methodology uses conventionally fabricated IDTs on a piezoelectric/optical material—lithium niobate (LN, $LiNbO_3$)—that is commonly used in optical waveguide and microfluidic applications. In contrast to SAW generated by pulsed lasers, typically used for material characterization (*15*), this IDT-based method presents a more conventional, easily used route for the generation of nanosecond-scale traveling SAW pulses without the need for optical equipment and permits the generation of high-amplitude substrate displacements for microfluidic manipulation.

SAW is profoundly useful for microscale manipulation because the length scale of the waves themselves is on the order of micrometers. Typical SAW wavelengths, 1 to 300 μm, are generated using frequencies between 10 and 1000 MHz (*16*, *17*). SAW is driven by conducting IDT structures on a piezoelectric substrate, where (at resonance) the mechanical displacements emanating from one set of finger pairs are reinforced by those from neighboring ones, with the resulting displacements maximized when $f = c_s/\lambda_{SAW}$, where c_s is the sound speed in the substrate. Compared to BAW transducers (*18*–*20*), SAW is especially suitable for microfluidic applications because it is generated on a planar surface, is readily integrated with channel structures, and generates an acoustic field only in desired locations (*17*). These advantages have been used in SAW applications, including cell patterning (*21*), interfacial manipulation (*22*, *23*), free surface translation (*24*, *25*), atomization (*26*, *27*), thin-film formation (*27*, *28*), particle and cell separation (*29*–*32*), fluid pumping (*33*), localized heating (*34*, *35*), and selective sorting (*31*, *36*).

This work represents a substantial evolution of acoustic microfluidics, where standing wave–induced acoustic forces can be confined not only across the width of the transducers as in conventional SAW but also along the direction of propagation. This method takes advantage of the small, microsecond-order TOF over which a SAW will propagate from one set of transducers to the opposing set, with TOF = d/c_s, where d is the characteristic distance over which a wave travels. When these IDTs are actuated by a pulse width with time t_p less than this characteristic TOF, the width of the overlapping region (w) where the traveling waves emanating from each set of IDTs intersect is a subset of the total distance between them, with $\frac{t_p}{TOF} \sim \frac{w}{d}$. This principle is shown in the conceptual diagram in Fig. 1A and the sketch in Fig. 1B. Figure 1C shows an example of a completed device, where a polydimethylsiloxane (PDMS) channel is used to contain a fluid volume with suspended particles.

RESULTS

Our analytical models and numerical simulations of this TOF regime closely mirror one another. Figure 2 shows both the simulated and modeled traveling waveform (Fig. 2A) and the resulting time-averaged displacements (Fig. 2B) from the intersection of two of these

[1]Pillar of Engineering Product Development, Singapore University of Technology and Design, Singapore 487372, Singapore. [2]Department of Mechanical and Aerospace Engineering, Monash University, Melbourne, Victoria 3800, Australia.
*Corresponding author. Email: adrian.neild@monash.edu (A.N.); aiye@sutd.edu.sg (Y.A.)

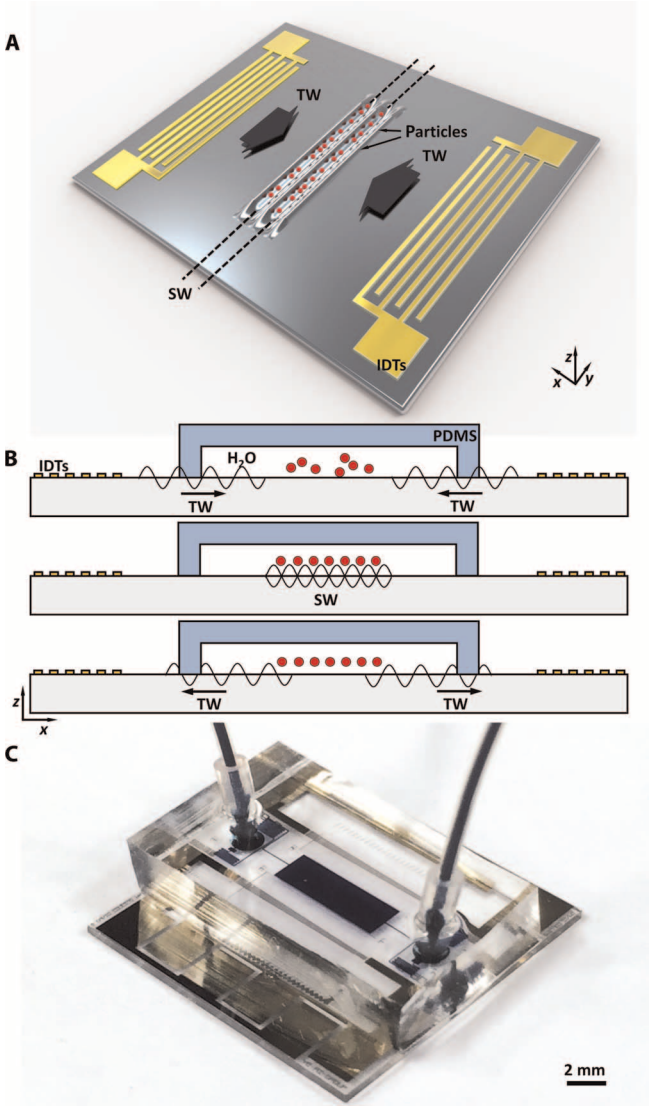

Fig. 1. Principle of TOF localized standing waves. (**A**) The opposing sets of IDTs are both actuated with a pulse length shorter than the TOF between them, resulting in traveling waves (TW) that constructively/destructively interfere where these two waves meet. (**B**) Over multiple pulses, the time-averaged effect of this localized standing wave (SW) yields a number of fixed nodal positions in the substrate, resulting in particle patterning in discrete locations where these pulsed waves intersect. (**C**) A PDMS channel is used to contain particles suspended in a fluid, which is replaced here with blue dye to better visualize the channel extents.

counterpropagating waves. The waveform shape of the propagating wave $\xi_x(x)$ can be analytically modeled by calculating the contributions from each finger pair in the set of IDTs over the length of the SAW pulse, given by

$$\xi_x(x) = \xi_0 \begin{cases} x - \frac{w_t}{2} & \text{for } x = \left[-\frac{w_t}{2} - \frac{w_x}{2}, -\frac{w_t}{2} + \frac{w_x}{2}\right] \\ 1 & \text{for } x = \left[-\frac{w_t}{2} + \frac{w_x}{2}, \frac{w_t}{2} - \frac{w_x}{2}\right] \\ 1 - \left(x + \frac{w_t}{2} - \frac{w_x}{2}\right) & \text{for } x = \left[\frac{w_t}{2} - \frac{w_x}{2}, \frac{w_t}{2} + \frac{w_x}{2}\right] \end{cases} \quad (1)$$

where ξ_0 is the initial SAW displacement, $w_t = c_s t_p$ is the applied pulse width, $w_x = N\lambda_{SAW}$ (both in units of length), and N is the number of finger pairs. The first and third terms account for the ramping regions on either end of the pulse, resulting from the incomplete resonance from a subset of the total number of finger pairs. The total pulse width (w) is equal to $w_t + w_x$ (for $w_t > w_x$) due to the contributions from all IDT finger pairs, where w is at least as large as w_x. For $w_t < w_x$, the maximum displacement amplitude is given by $\xi_x^{max} = w_t/w_x$, shown by the green lines in Fig. 2A. The modeled time-averaged waveform shape is computed from the autocorrelation (self-intersection) of the transient modeled waveform, with $\xi_x^{avg}(x) = \xi_x(x)*\xi_x(x)$, and compares favorably to the simulated time-averaged displacement (Fig. 2B). Figure 2C demonstrates the sequence of stages in the development of a spatially localized intersecting SAW in full 3D simulation of a SAW emanating from opposing sets of IDTs on a piezoelectric LN substrate, including the initial generation, propagation, intersection, and continuous propagation after intersection. The maximum displacement amplitude at complete intersection for 5T, 10T, and 20T pulses are shown in Fig. 2D; note the graded amplitude decay at either end of this region, a feature that arises from the partial reinforcement of displacements for the initial few periods when more than one finger pair is used in a set of IDTs. It follows that the maximum amplitude is only reached for a given pulse when the pulse time exceeds the time required for a SAW to traverse the width of the IDTs. Figure 2A shows these effects, where, for a six–finger pair device, there are six local maxima before reaching maximum amplitude at the leading (and trailing) edges except for the case in which a pulse time of 5T is applied, in which case the steady-state maximum is never reached. That Eq. 1 is a good match for the simulation results in Fig. 2A, which emerge directly from applying an AC boundary condition to our electrodes on a simulated LN substrate, is a good verification of this model.

Figure 3A demonstrates the existence of discrete patterning locations in an experimental setup, actuated by opposing sets of six–finger pair IDTs (7-mm aperture) with a time-averaged applied power of 0.35 W (with a duty cycle of 0.1 and a period 10 times the pulse width). Figure 3A shows larger localized patterning regions for both longer pulse times and larger numbers of finger pairs, as expected from Eq. 1. Continuous SAW results in acoustic nodal positions throughout the width of the microfluidic channel (*37*–*39*), whereas pulsed nanosecond-scale actuation only results in particle patterning in the locations where the intersecting waves overlap (the localized standing wave region), leaving particles outside of this region largely unaffected. Graphs associated with each experimental image show predicted minimum displacement locations, corresponding to areas where 2-μm particles collect (MagSphere), where these analytical models incorporate the attenuation of the acoustic beam as it travels along the substrate/fluid interface and display the time-averaged displacement relative to that before exposure to the fluid. The dimensions of the predicted region compare favorably for smaller pulse lengths, although the observed patterning region is somewhat smaller than the full extent of the region for which a partial standing wave exists at longer pulse lengths. This illustrates the effect of acoustic attenuation arising from a water-loaded SAW: With an attenuation length of ~500 μm, the magnitude of each propagating 40-μm-wavelength SAW is reduced to 13% of the original one at the channel center and is less than 5% by the end of the predicted patterning region (at approximately y = 550 μm in the case of a 300-ns pulse). The dotted lines in Fig. 3A represent the condition where the local average displacement minima are less than $0.2\xi_0$,

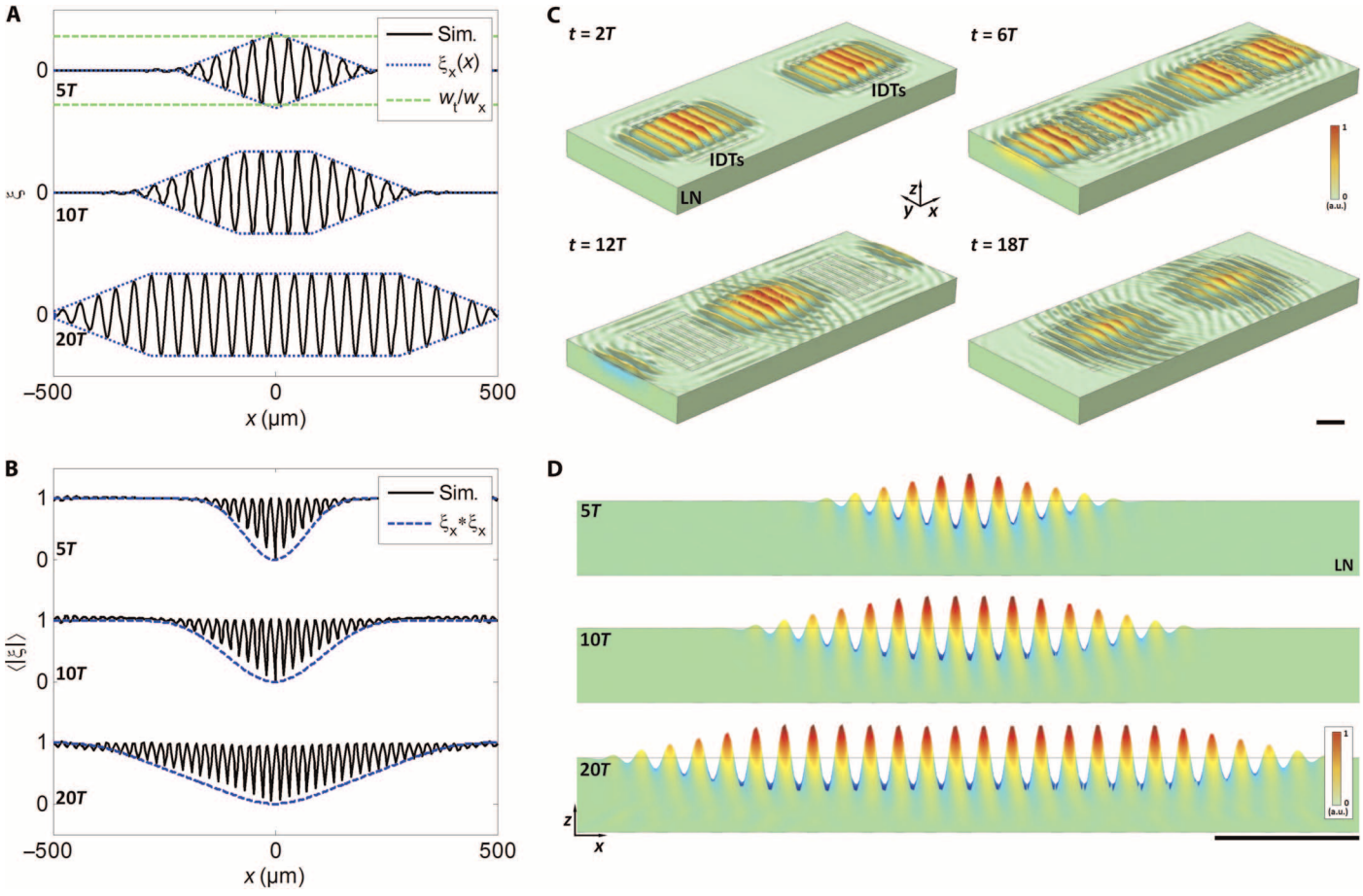

Fig. 2. Simulated and modeled response to SAW pulses on the order of 100 ns. (**A**) The simulated shapes of the transient traveling SAW pulses closely match the model in Eq. 1 for actuation by six–finger pair IDTs, with pulse time periods (*t*p) of 5*T*, 10*T*, and 20*T*, where $T = \lambda_{SAW}/c_s$, which is the time it takes for a traveling SAW to traverse one SAW wavelength (here simulated with λ_{SAW} = 40 μm). (**B**) The simulated time-averaged substrate displacements closely match the modeled displacement curves for these same finger pair and *T* values, here showing the convolution $\xi_x(x)*\xi_x(x)$ from Eq. 1. (**C**) The time-averaged nodal positions result from the combination of transient pulses, here showing an intersection sequence using a full 3D simulation during SAW generation (*t* = 2*T*), SAW propagation (*t* = 6*T*), intersection (*t* = 12*T*), and continuing propagation (*t* = 18*T*). See movie S2 for time-dependent simulations. (**D**) The time-averaged minimum displacement locations in (B) correspond to the nodal positions presented here, which show the instantaneous maximum displacements at transient wave intersection. Scale bars, 100 μm.

which yields a consistent and reasonable match for the dimensions in which strong patterning occurs for the given applied power and channel dimensions used here. Although local minima exist outside this region, these prove insufficient for the purpose of producing strong and reproducible patterning phenomena, owing to the relative weakness of the local acoustic field. These patterning regions are demonstrated in a continuous flow in movie S4.

An important consideration in acoustic microfluidics is the influence of the traveling waves themselves on particle behavior. This is not a significant factor in this instance due to the size of the particles relative to that of the fluid wavelength. The reflections in the vicinity of the particle become increasingly directional and of larger magnitude with increasing particle dimensions, where the force scaling changes from an $F{\sim}R^6/F{\sim}R^3$ relationship [depending on the viscosity of the surrounding medium (*40*)], where *F* is the acoustic force and *R* is the particle radius, to a more complex relationship as the particle size approaches the acoustic wavelength (*41*, *42*). Although the size of the viscous boundary layer varies with fluid density and viscosity (*43*), which in turn influences the particle size at which the traveling wave forces become significant for the purposes of particle translation, this transition has been experimentally determined to occur in the vicinity of $\kappa \approx 1.3$ to 1.4 for polystyrene particles in water (*44*–*46*). Here, $\kappa = \pi d/\lambda_f$, where *d* is the particle diameter and λ_f is the wavelength in the fluid, yielding a maximum diameter (d_{max}) of 6 and 12 μm for the 40- and 80-μm wavelengths (λ_{SAW}), respectively, used in this work. The traveling wave force does not significantly modify particle positions below such dimensions, and particles will be translated toward the channel center at dimensions above these. For the 2- and 3-μm particles used in this work, these equate to κ values of 0.4 and 0.6, respectively, which accordingly failed to demonstrate directional particle motions arising from the traveling wave force.

The development of the localized field is analyzed in Fig. 3B, which shows the mean fluorescence intensity of the particles as they are being patterned across the simulated region shown in Fig. 3C (see movie S1). The primary aggregation of particles occurs in the localized standing

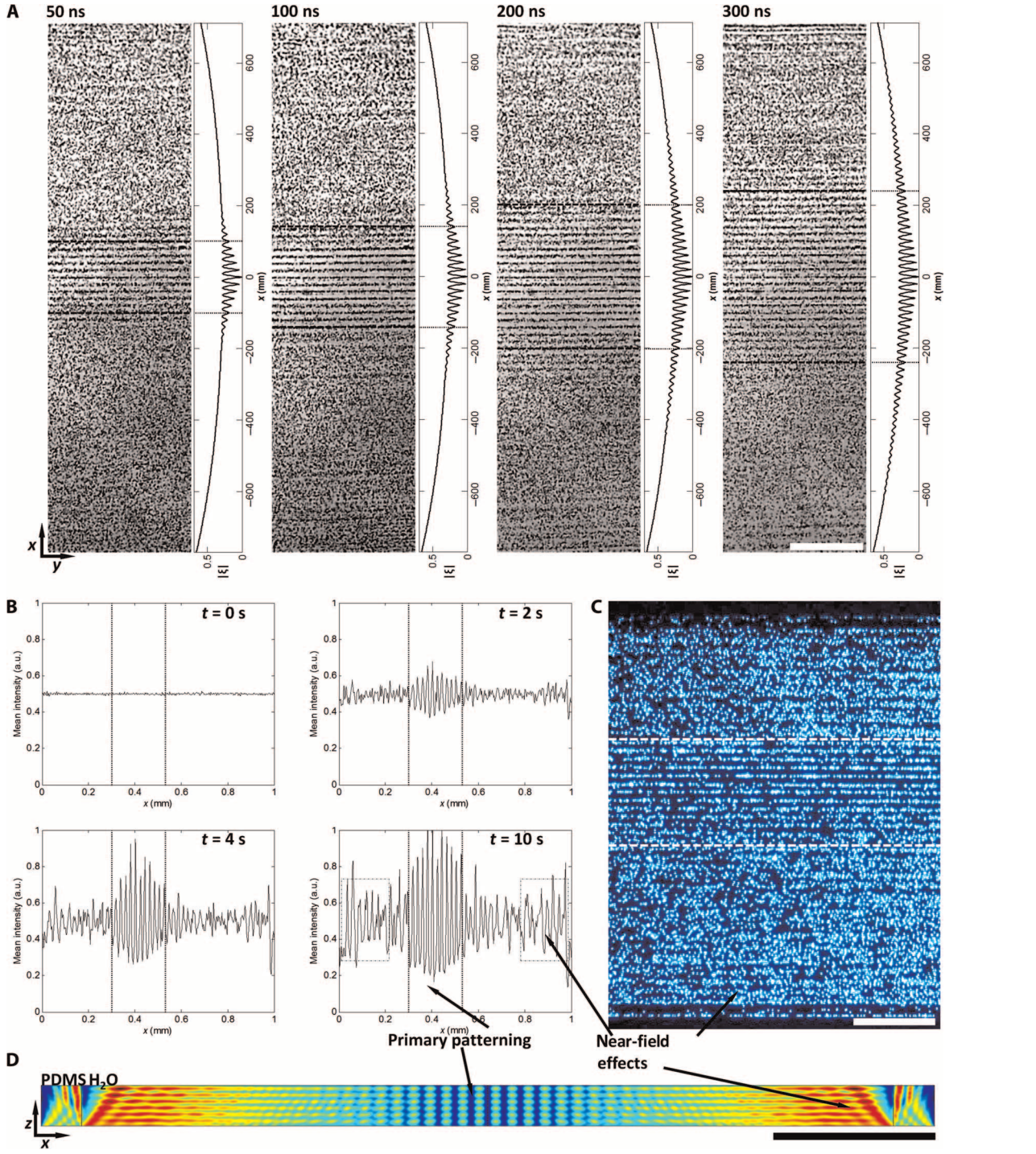

Fig. 3. Experimental particle patterning actuated by continuous and sub-TOF regime pulsed SAW. (**A**) In contrast to conventionally applied acoustic fields, applying pulse lengths with t_p < TOF results in the time-averaged standing wave locations only where the two incident waves overlap, here with t_p = 50, 100, 200, and 300 ns (approximately 5*T*, 10*T*, 20*T*, and 30*T*), driven by 40-μm six–finger pair transducers at 96 MHz, visualized with 2-μm particles in a 2-mm-wide channel after 5 s of pulsed excitation (time-averaged applied power = 0.35 W). These patterns correspond to the predicted patterning locations at time-averaged minimum displacement conditions, especially for smaller time-averaged minima (dotted lines correspond to conditions where |ξ| minima are less than 0.2). Continuous patterning is demonstrated in movie S4. (**B**) During pattern development in a 1-mm-wide channel, 3-μm primary particle patterns result from the combination of the intersecting 100-ns pulsed traveling waves (between dotted lines). a.u., arbitrary units. (**C**) Mean intensity along the *x* direction is assayed in the region (for *t* = 10 s) from movie S1. (**D**) The appearance of secondary near-field patterning [dash-dot boxes in (B)] results from diffraction in the vicinity of the acoustic impedance discontinuity at the channel wall boundary shown here. Scale bars, 200 μm.

wave region, whereas secondary near-field patterning is observed to develop over longer time scales (dash-dot lines in Fig. 3B). We find that the emergence of this effect can be explained by the generation of time-averaged pressure amplitude patterns in the vicinity of the acoustic property discontinuity at the PDMS/fluid boundary (see Fig. 3D). This 2D numerical simulation, a video of which is shown in movie S2, models the solid/fluid acoustic interactions in a pulsed field. The spherical propagation of acoustic displacements in the vicinity of this interface according to the Huygens-Fresnel principle results in near-field diffraction and time-averaged regions of lower acoustic energy toward which particles will preferentially migrate (*43*), although the magnitude of these variations is less pronounced than that in the central patterning region, which has larger acoustic pressure gradients. This model (pictured at $t = 41T$) simulates the interaction of a SAW emanating from a six–finger pair set of IDTs actuated with a pulse lasting $10T$ (~100 ns) along a piezoelectric LN substrate and the effects of the PDMS domain at the channel periphery. The top surface of the fluid domain, the channel roof, is imposed with a PDMS impedance boundary condition, which is sufficient because the PDMS domain is much larger than the channel height, whereas the 50-μm PDMS walls are explicitly simulated. The effect of a physical PDMS boundary over the fluid domain is minimal, resulting in a small amount of reflection due to the fractional acoustic impedance difference between water and PDMS and thus a degree of acoustic patterning in the *z* direction, although the magnitude of this effect is secondary to that of primary patterning.

Patterning in the TOF regime is not limited to the generation of unitary localized standing wave fields. Figure 4 shows the generation of three separate time-averaged patterning regions by using a pulse period that is less than the amount of time the entire traveling wave pulse takes to traverse the width of the channel (here, a 75-ns pulse with a 200-ns period was used, which is less than the 254-ns TOF + 75-ns pulse length of the 1-mm channel). The instantaneous, analytically modeled, and interfering waves, as well as their time-averaged displacements, are shown in movie S3. The modeled minimum displacements in Fig. 4C correlate with the observed particle aggregation locations, measured from the mean fluorescence intensity in Fig. 4 (A and B). Here, the channel is displaced (90 μm vertically) from the midpoint between opposing transducers to demonstrate the independence of the patterning region from the channel dimensions; because the standing wave locations are substrate-bound, the patterning locations can be arbitrarily determined with respect to the channel.

In the cases examined so far, the patterning regions have been symmetrical about the midpoint between the opposing sets of IDTs: This is where counterpropagating waves intersect when each set of transducers is actuated simultaneously. However, the TOF-induced patterning regions can also be applied at arbitrary locations along the propagation direction by independently controlling the times at which each set of transducers is actuated. By applying a triggered delay to the 100-ns, 48-MHz pulse to one of two sets of 80-μm six–finger pair IDTs in a 3-mm-wide channel in Fig. 5A, we demonstrate that the patterning locations can be generated independently of the channel position on the SAW device. Here, the traveling SAW propagating along the *x* direction from the upper set of IDTs generated hundreds of nanoseconds before and after that from the lower set, resulting in highly accurate patterning region shifts. Patterning localization can similarly be extended into the *y* direction by using a SAW device architecture where the acoustic wavelength varies across the IDT aperture. Figure 1C shows such a device, where λ_{SAW} varies between 40 and 80 μm, corresponding to resonant frequency conditions between 48 and 96 MHz (larger wavelengths correspond to lower frequencies). Applying 100-ns pulses at frequencies in this range results in localized patterning only where a SAW is produced, as shown in Fig. 5B, where the patterning region is shifted laterally along the device aperture for 55-, 65-, 75-, and 85-MHz frequencies (corresponding to wavelengths of 71, 60, 52, and 46 μm). However, the localization along the *y* direction (~1 mm) is not as discrete as that along the propagation direction (~100 μm) in this implementation, given the large device aperture (10 mm) and the small number of finger pairs (*6*) that result in a wide transmission bandwidth (*47*); the localization in this direction could be improved with larger numbers of finger pairs and/or larger wavelength gradients (using smaller apertures and/or wider frequency ranges), although as a trade-off, the width of the *x* direction patterning region would increase in line with Eq. 1 for an increasing number of finger pairs.

Although the extent of the patterning regions is on the order of 100 μm at a minimum for wavelengths on the order of tens of micrometers and thus by itself limits the application of these patterning regions for manipulation of individual particles or cells in concentrated solutions, this can be somewhat circumvented via the fine-grained control that is achievable within the patterning region itself, where phase shifts can result in translated time-averaged nodal positions (*48*, *49*). Figure 5C demonstrates the shift in nodal positions with the application of a phase-shifted, 48-MHz, 100-ns pulse in a device with a λ_{SAW} of 80 μm. Applying a phase delay of $\Delta\varphi = 180°$ results in an inversion of the nodal/antinodal positions compared to $\Delta\varphi = 0°$, for example, and the gradual shift between these two cases results in total translation/nodal position differences that are smaller than the acoustic wavelength.

DISCUSSION

The effect of attenuation at the LN/water interface, which results from the transfer of energy from the solid substrate to the coupled fluid, with an attenuation length (over which the initial displacement amplitude decays to $1/e$ of its initial value) of $12.8\,\lambda_{SAW}$ is yet to be discussed (*31*, *50*). For the case tested, this means that each incoming 40-μm wave will have attenuated to approximately 38% of its initial value at the center of a 1-mm channel but approximately 14% at the center of a 2-mm channel. Not surprisingly, this attenuation has little effect on the expected nodal positions where particles aggregate for a smaller channel width but has considerable effect for larger channels. Note that patterning is demonstrated across the width of the 1-mm channel in Fig. 4A, whereas longer pulse lengths result in smaller-than-expected patterning regions for the wider channel in Fig. 3A. However, even a standing wave at a fractional value of its initial intensity should still eventually lead to particle migration, albeit at a lower rate. However, amplitude attenuation in the fluid itself presents a potentially more potent effect on particle translation, where the propagation of a high-frequency acoustic wave through a dispersive medium, such as water, generates a body force in the direction of propagation (*50*). This effect can be reduced by minimizing the body force gradients that give rise to acoustic streaming, at their strongest at the edge of the SAW beam, and reducing the channel height where appropriate (*28*, *51*). Acoustic gradients can be ameliorated for patterning applications, as it has been in this work, by using channel widths smaller than the IDT aperture (3.2 and 3.6 mm for the 40-μm device in Fig. 3B). This is not necessarily required, where streaming is similarly not a noticeable concern even

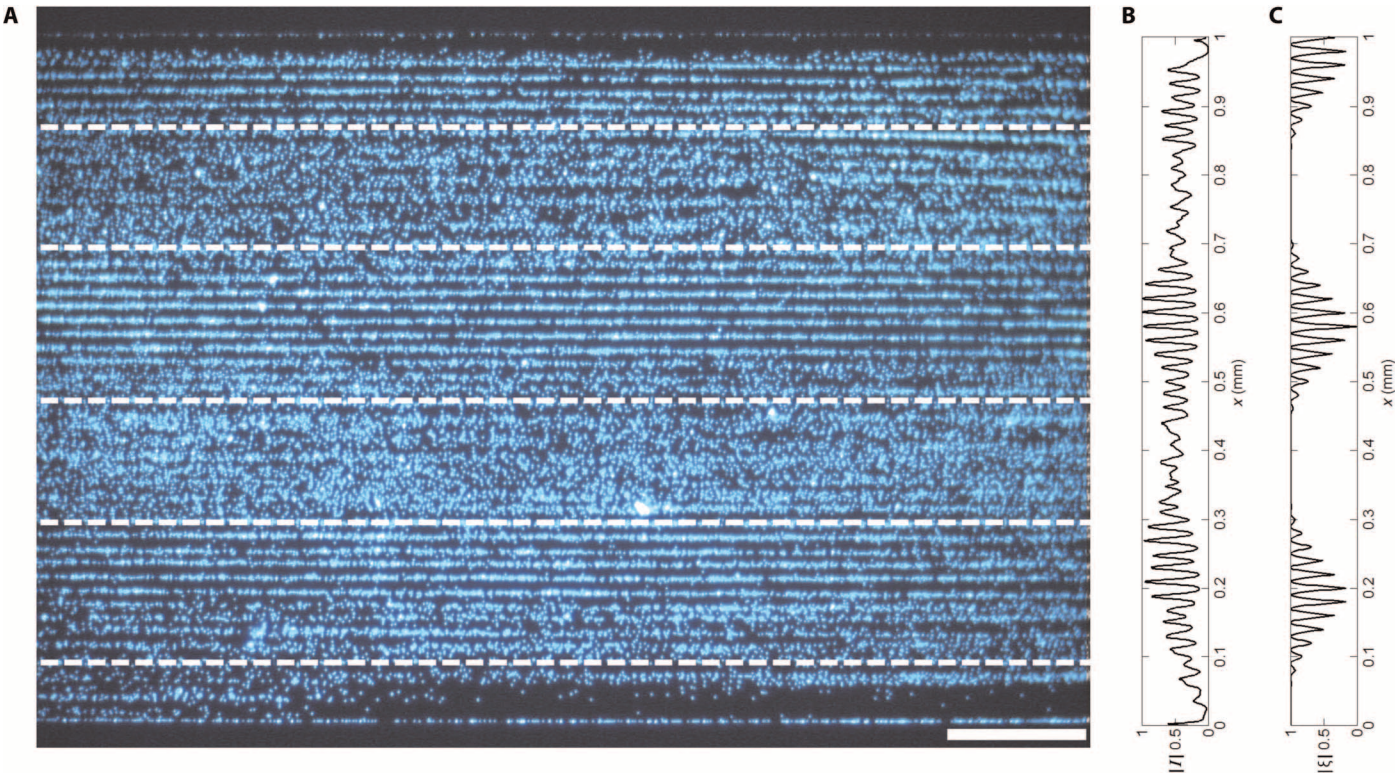

Fig. 4. Generation of multiple discrete patterning regions. (**A**) The application of a 75-ns pulse with a 200-ns period, which is less than the minimum time it takes for a complete wave to pass across the 1-mm channel (the channel's 254-ns TOF plus the 75-ns pulse period), generates symmetric standing wave regions as visualized with patterned 3-μm particles. (**B** and **C**) The measured mean intensity across the width of the channel (B), corresponding to the predicted locations of minimum time-averaged displacement (C). Scale bar, 200 μm.

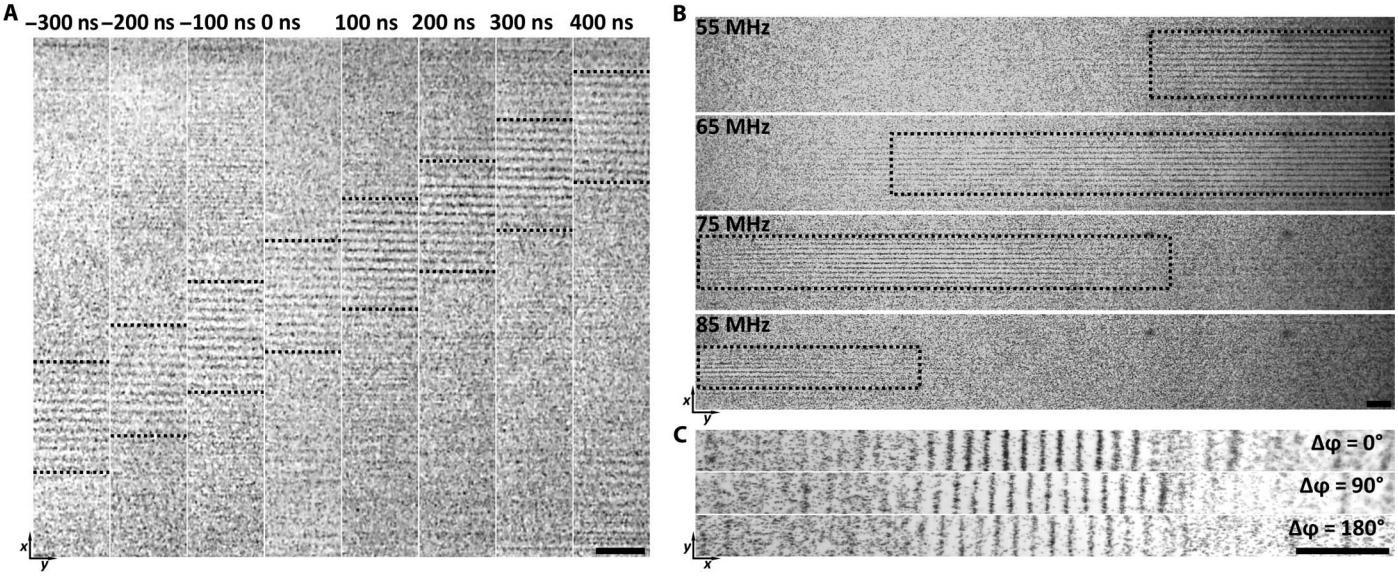

Fig. 5. 2D patterning control. (**A**) The patterning region in the direction of propagation (the *x* direction) can be arbitrarily determined through the imposition of a time-delayed pulse, where the pulse traveling from the top of the device is delayed by the value shown. (**B**) The patterning regions in the *y* direction (in dashed boxes) can similarly be modified using a SAW device whose wavelength changes along the *y* direction (here between 40 and 80 μm; device shown in Fig. 1C). All other results are for nonslanted IDT designs. (**C**) The patterning of nodal positions within the patterning region can also be shifted by imposing a phase shift Δφ to one of the opposing sets of transducers. All particles are 2 μm. Scale bars, 200 μm.

with the use of slanted-finger IDTs, as is the case in Fig. 5C, where the SAW beam width is smaller than that of the channel. This is partly due to the graded drop-off in displacement magnitude with this transducer type (*52*).

Given the wide range of activities that are already accomplished with SAW, the use of nanosecond-scale pulses to generate locality along the direction of propagation and across the width of the transducers represents a conceptually simple but significant evolution in the dexterity that is possible using microscale acoustic fields. Reducing the width of the region over which a standing wave is formed permits localized trapping in a manner more analogous to optical tweezers, leaving surrounding regions unaffected. Phase shifts between opposing transducers combined with the imposition of an additional orthogonal SAW allow for selective and fully 2D particle and cell manipulation. Moreover, given the wide use of SAW for optical and mechanical manipulation, the ability to further localize acoustic fields presents a new avenue for the fine-tuned generation of highly local SAW displacements.

MATERIALS AND METHODS

Numerical simulation

The numerical simulation was performed using COMSOL v5.0 (see Fig. 2, C and D). A time-dependent transient 2D model was used to simulate waveforms by applying an AC signal to regions representing the IDT finger pairs on a piezoelectric substrate. The stiffness, coupling coefficient, and electrical permittivity matrices were rotated to correspond to the 128° *y*-cut *x*-propagating LN crystal used experimentally. The maximum mesh size dimension was $\lambda_{SAW}/10$.

SAW devices

IDTs are composed of a conductive 200-nm Al or Au layer on a 7-nm Cr adhesion layer and patterned on a piezoelectric LN substrate using the lift-off process after evaporative metal deposition. The width of each metal strip is equal to $\lambda_{SAW}/4$, 10 μm for λ_{SAW} = 40 μm, 20 μm for λ_{SAW} = 80 μm, and linearly graded between 10 and 20 μm for the 40- to 80-μm slanted-finger IDT device. A finished device was produced by bonding a PDMS microchannel to the substrate after exposure to an air plasma (Harrick Plasma PDC-32G; 1000 mtorr, 18 W). This bonded microchannel (1 mm wide and 20 μm high, 2 mm wide and 40 μm high, or 3 mm wide and 60 μm high) incorporated an air channel over the IDTs and a small, 50-μm-thick PDMS wall between the air- and fluid-filled sections to minimize attenuation before the fluid channel. These devices were actuated with a signal generator (AnaPico APGEN3000HC and Tektronix AFG3102C) and an amplifier (Ophir 5084 and Empower 1100) on a custom-printed, 3D-printed mount with spring-loaded probes making contact with the electrode pads and visualized with an inverted microscope through the transparent substrate. Phase shifts and time delays at 48 MHz (for the results in Fig. 5, A and C) were readily achieved in the two-channel Tektronix unit, which uses a common reference oscillator. A blank piece of LN was used to eliminate birefringence through this optically polarizing material.

SUPPLEMENTARY MATERIALS

Supplementary material for this article is available at http://advances.sciencemag.org/cgi/content/full/2/7/e1600089/DC1

movie S1. Development of localized acoustic patterning region.

movie S2. Numerical simulation of pulsed SAW, including 2D and 3D models of the piezoelectric substrate and a model of the acoustofluidic interaction.

movie S3. Analytical model of sub-TOF regime SAW.

movie S4. Generation of time-averaged localized patterning regions using 50-, 100-, 200-, and 300-ns pulses.

REFERENCES AND NOTES

1. N. Courjal, S. Benchabane, J. Dahdah, G. Ulliac, Y. Gruson, V. Laude, Acousto-optically tunable lithium niobate photonic crystal. *Appl. Phys. Lett.* **96**, 131103 (2010).
2. L. Kuhn, M. Dakss, P. Heidrich, B. Scott, Deflection of an optical guided wave by a surface acoustic wave. *Appl. Phys. Lett.* **17**, 265–267 (1970).
3. J.-H. Sun, T.-T. Wu, Propagation of surface acoustic waves through sharply bent two-dimensional phononic crystal waveguides using a finite-difference time-domain method. *Phys. Rev. B* **74**, 174305 (2006).
4. J.-C. Beugnot, S. Lebrun, G. Pauliat, H. Maillotte, V. Laude, T. Sylvestre, Brillouin light scattering from surface acoustic waves in a subwavelength-diameter optical fibre. *Nat. Commun.* **5**, 5242 (2014).
5. S. Kapfinger, T. Reichert, S. Lichtmannecker, K. Müller, J. J. Finley, A. Wixforth, M. Kaniber, H. J. Krenner, Dynamic acousto-optic control of a strongly coupled photonic molecule. *Nat. Commun.* **6**, 8540 (2015).
6. J. Luo, F. Pan, P. Fan, F. Zeng, D. P. Zhang, Z. H. Zheng, G. X. Liang, Cost-effective and high frequency surface acoustic wave filters on ZnO: Fe/Si for low-loss and wideband application. *Appl. Phys. Lett.* **101**, 172909 (2012).
7. F. Bender, R. E. Mohler, A. J. Ricco, F. Josse, Identification and quantification of aqueous aromatic hydrocarbons using SH-surface acoustic wave sensors. *Anal. Chem.* **86**, 1794–1799 (2014).
8. M. Miansari, A. Qi, L. Y. Yeo, J. R. Friend, Vibration-induced deagglomeration and shear-induced alignment of carbon nanotubes in air. *Adv. Funct. Mater.* **25**, 1014–1023 (2014).
9. Z. Ma, J. Guo, Y. J. Liu, Y. Ai, The patterning mechanism of carbon nanotubes using surface acoustic waves: The acoustic radiation effect or the dielectrophoretic effect. *Nanoscale* **7**, 14047–14054 (2015).
10. J. Shi, D. Ahmed, X. Mao, S.-C. S. Lin, A. Lawita, T. J. Huang, Acoustic tweezers: Patterning cells and microparticles using standing surface acoustic waves (SSAW). *Lab Chip* **9**, 2890–2895 (2009).
11. X. Ding,S.-C. S. Lin, B. Kiraly, H. Yue, S. Li, I.-K. Chiang, J. Shi, S. J. Benkovic, T. J. Huang, On-chip manipulation of single microparticles, cells, and organisms using surface acoustic waves. *Proc. Natl. Acad. Sci. U.S.A.* **109**, 11105–11109 (2012).
12. C. R. P. Courtney, C. E. M. Demore, H. Wu, A. Grinenko, P. D. Wilcox, S. Cochran, B. W. Drinkwater, Independent trapping and manipulation of microparticles using dexterous acoustic tweezers. *Appl. Phys. Lett.* **104**, 154103 (2014).
13. A. L. Bernassau, P. G. A. MacPherson, J. Beeley, B. W. Drinkwater, D. R. S. Cumming, Patterning of microspheres and microbubbles in an acoustic tweezers. *Biomed. Microdevices* **15**, 289–297 (2013).
14. F. J. R. Schülein, E. Zallo, P. Atkinson, O. G. Schmidt, R. Trotta, A. Rastelli, A. Wixforth, H. J. Krenner, Fourier synthesis of radiofrequency nanomechanical pulses with different shapes. *Nat. Nanotechnol.* **10**, 512–516 (2015).
15. Y. Orphanos, V. Dimitriou, E. Kaselouris, E. Bakarezos, N. Vainos, M. Tatarakis, N. A. Papadogiannis, An integrated method for material properties characterization based on pulsed laser generated surface acoustic waves. *Microelectron. Eng.* **112**, 249–254 (2013).
16. R. J. Shilton, M. Travagliati, F. Beltram, M. Cecchini, Nanoliter-droplet acoustic streaming via ultra high frequency surface acoustic waves. *Adv. Mater.* **26**, 4941–4946 (2014).
17. L. Y. Yeo, J. R. Friend, Surface acoustic wave microfluidics. *Annu. Rev. Fluid Mech.* **46**, 379–406 (2014).
18. P. Hahn, I. Leibacher, T. Baasch, J. Dual, Numerical simulation of acoustofluidic manipulation by radiation forces and acoustic streaming for complex particles. *Lab Chip* **15**, 4302–4313 (2015).
19. P. Mishra, M. Hill, P. Glynne-Jones, Deformation of red blood cells using acoustic radiation forces. *Biomicrofluidics* **8**, 034109 (2014).
20. M. Caleap, B. W. Drinkwater, Acoustically trapped colloidal crystals that are reconfigurable in real time. *Proc. Natl. Acad. Sci. U.S.A.* **111**, 6226–6230 (2014).
21. D. J. Collins, B. Morahan, J. Garcia-Bustos, C. Doerig, M. Plebanski, A. Neild, Two-dimensional single-cell patterning with one cell per well driven by surface acoustic waves. *Nat. Commun.* **6**, 8686 (2015).
22. D. J. Collins, T. Alan, K. Helmerson, A. Neild, Surface acoustic waves for on-demand production of picoliter droplets and particle encapsulation. *Lab Chip* **13**, 3225–3231 (2013).
23. L. Schmid, T. Franke, SAW-controlled drop size for flow focusing. *Lab Chip* **13**, 1691–1694 (2013).

24. Y. Ai, B. L. Marrone, Droplet translocation by focused surface acoustic waves. *Microfluid. Nanofluid.* **13**, 715–722 (2012).
25. H. Li, J. R. Friend, L. Y. Yeo, Surface acoustic wave concentration of particle and bioparticle suspensions. *Biomed. Microdevices* **9**, 647–656 (2007).
26. A. Winkler, S. M. Harazim, S. B. Menzel, H. Schmidt, SAW-based fluid atomization using mass-producible chip devices. *Lab Chip* **15**, 3793–3799 (2015).
27. D. J. Collins, O. Manor, A. Winkler, H. Schmidt, J. R. Friend, L. Y. Yeo, Atomization off thin water films generated by high-frequency substrate wave vibrations. *Phys. Rev. E* **86**, 056312 (2012).
28. A. R. Rezk, O. Manor, J. R. Friend, L. Y. Yeo, Unique fingering instabilities and soliton-like wave propagation in thin acoustowetting films. *Nat. Commun.* **3**, 1167 (2012).
29. D. J. Collins, T. Alan, A. Neild, Particle separation using virtual deterministic lateral displacement (vDLD). *Lab Chip* **14**, 1595–1603 (2014).
30. P. Li, Z. Mao, Z. Peng, L. Zhou, Y. Chen, P.-H. Huang, C. I. Trucia, J. J. Drabick, W. S. El-Diery, M. Dao, S. Suresh, T. J. Huang, Acoustic separation of circulating tumor cells. *Proc. Natl. Acad. Sci. U.S.A.* **112**, 4970–4975 (2015).
31. D. J. Collins, A. Neild, Y. Ai, Highly focused high-frequency travelling surface acoustic waves (SAW) for rapid single-particle sorting. *Lab Chip* **16**, 471–479 (2015).
32. Y. Ai, C. K. Sanders, B. L. Marrone, Separation of *Escherichia coli* bacteria from peripheral blood mononuclear cells using standing surface acoustic waves. *Anal. Chem.* **85**, 9126–9134 (2013).
33. M. B. Dentry, J. R. Friend, L. Y. Yeo, Continuous flow actuation between external reservoirs in small-scale devices driven by surface acoustic waves. *Lab Chip* **14**, 750–758 (2014).
34. B. H. Ha, K. S. Lee, G. Destgeer, J. Park, J. Seung, J. H. Jung, J. H. Shin, H. J. Sung, Acousto-thermal heating of polydimethylsiloxane microfluidic system. *Sci. Rep.* **5**, 11851 (2015).
35. R. J. Shilton, V. Mattoli, M. Travagliati, M. Agostini, A. Desii, F. Beltram, M. Cecchini, Rapid and controllable digital microfluidic heating by surface acoustic waves. *Adv. Funct. Mater.* **25**, 5895–5901 (2015).
36. L. Ren, Y. Chen, P. Li, Z. Mao, P.-H. Huang, J. Rufo, F. Guo, L. Wang, J. P. McCoy, S. J. Levine, T. J. Huang, A high-throughput acoustic cell sorter. *Lab Chip* **15**, 3870–3879 (2015).
37. C. Devendran, N. R. Gunasekara, D. J. Collins, A. Neild, Batch process particle separation using surface acoustic waves (SAW): Integration of travelling and standing SAW. *RSC Adv.* **6**, 5856–5864 (2016).
38. F. Guo, P. Li, J. B. French, Z. Mao, H. Zhao, N. Nama, J. R. Fick, S. J. Benkovic, T. J. Huang, Controlling cell–cell interactions using surface acoustic waves. *Proc. Natl. Acad. Sci. U.S.A.* **112**, 43–48 (2015).
39. Y. Chen, S. Li, Y. Gu, P. Li, X. Ding, L. Wang, J. P. McCoy, S. J. Levine, T. J. Haang, Continuous enrichment of low-abundance cell samples using standing surface acoustic waves (SSAW). *Lab Chip* **14**, 924–930 (2014).
40. A. A. Doinikov, Acoustic radiation force on a spherical particle in a viscous heat-conducting fluid. II. Force on a rigid sphere. *J. Acoust. Soc. Am.* **101**, 722–730 (1997).
41. T. Hasegawa, K. Yosioka, Acoustic-radiation force on a solid elastic sphere. *J. Acoust. Soc. Am.* **46**, 1139–1143 (1969).
42. T. Hasegawa, K. Yosioka, Acoustic radiation force on fused silica spheres, and intensity determination. *J. Acoust. Soc. Am.* **58**, 581–585 (1975).
43. M. Settnes, H. Bruus, Forces acting on a small particle in an acoustical field in a viscous fluid. *Phys. Rev. E* **85**, 016327 (2012).
44. Z. Ma, D. J. Collins, Y. Ai, Detachable acoustofluidic system for particle separation via a travelling surface acoustic wave. *Anal. Chem.* **88**, 5316–5323 (2016).
45. V. Skowronek, R. W. Rambach, L. Schmid, K. Haase, T. Franke, Particle deflection in a poly(dimethylsiloxane) microchannel using a propagating surface acoustic wave: Size and frequency dependence. *Anal. Chem.* **85**, 9955–9959 (2013).
46. G. Destgeer, B. H. Ha, J. H. Jung, A. Alazazam, H. J. Sung, Microchannel anechoic corner for size-selective separation and medium exchange via traveling surface acoustic waves. *Anal. Chem.* **87**, 4627–4632 (2015).
47. D. Morgan, *Surface Acoustic Wave Filters: With Applications to Electronic Communications and Signal Processing* (Academic Press, Cambridge, ed. 2, 2010).
48. N. D. Orloff, J. R. Dennis, M. Cecchini, E. Schonbrun, E. Rocas, Y. Wang, D. Novotny, R. W. Simmonds, J. Moreland, I. Takeuchi, J. C. Booth, Manipulating particle trajectories with phase-control in surface acoustic wave microfluidics. *Biomicrofluidics* **5**, 44107–441079 (2011).
49. C. R. Courtney, C.-K. Ong, B. W. Drinkwater, A. L. Bernassau, P. D. Wilcox, D. R. S. Cumming, Manipulation of particles in two dimensions using phase controllable ultrasonic standing waves. *Proc. R. Soc. London Ser. A*, rspa20110269 (2011).
50. M. B. Dentry, L. Y. Yeo, J. R. Friend, Frequency effects on the scale and behavior of acoustic streaming. *Phys. Rev. E* **89**, 013203 (2014).
51. D. J. Collins, Z. Ma, Y. Ai, Highly localized acoustic streaming and size-selective submicrometer particle concentration using high frequency microscale focused acoustic fields. *Anal. Chem.* **88**, 5513–5522 (2016).
52. R. W. Rambach, J. Taiber, C. M. L. Scheck, C. Meyer, J. Reboud, J. M. Cooper, T. Franke, Visualization of surface acoustic waves in thin liquid films. *Sci. Rep.* **6**, 21980 (2016).

Acknowledgments

Funding: We acknowledge the support received from the Singapore University of Technology and Design (SUTD)–Massachusetts Institute of Technology (MIT) International Design Center (IDG11300101) and SUTD Start-up Research Grant (SREP13053) awarded to Y.A. **Author contributions:** D.J.C. developed the concept, performed the experiments, created analytical models, and wrote the manuscript. Z.M. performed preliminary experiments. C.D. performed numerical modeling. J.W.N. helped with the device fabrication. A.N. and Y.A. helped shape experiments and modeling, analyzed the data, interpreted the results, and revised the manuscript. All authors read and approved the completed manuscript. **Competing interests:** The authors declare that they have no competing interests. **Data and materials availability:** All data needed to evaluate the conclusions in the paper are present in the paper and/or the Supplementary Materials. Additional data related to this paper may be requested from the authors.

Submitted 19 January 2016
Accepted 14 June 2016
Published 13 July 2016
10.1126/sciadv.1600089

Citation: D. J. Collins, C. Devendran, Z. Ma, J. W. Ng, A. Neild, Y. Ai, Acoustic tweezers via sub–time-of-flight regime surface acoustic waves. *Sci. Adv.* **2**, e1600089 (2016).